PERGAMON

International Journal of Heat and Mass Transfer 41 (1998) 3037–3054

International Journal of HEAT and MASS TRANSFER

Multi-dimensional modeling of thin liquid films and spray–wall interactions resulting from impinging sprays

Donald W. Stanton*, Christopher J. Rutland

Engine Research Center, Mechanical Engineering Department, University of Wisconsin—Madison, 1500 Engineering Dr., Madison, WI 53706, U.S.A.

Received 10 October 1997; in final form 14 January 1998

Abstract

The focus of this work is to formulate and validate a multi-dimensional, fuel film model to help account for the fuel distribution during combustion in internal combustion engines. Spray–wall interaction and spray–film interaction are also incorporated into the model. The fuel film model simulates thin fuel film flow on solid surfaces of arbitrary configuration. This is achieved by solving the continuity, momentum, and energy equations for the two-dimensional film that flows over a three-dimensional surface. The major physical processes considered in the model include mass and momentum contributions to the film due to spray drop impingement, splashing effects, various shear forces, piston acceleration, dynamic pressure effects, gravity driven flow, conduction, and convective heat and mass transfer. In order to adequately represent the drop interaction process, impingement regimes and post-impingement behavior have been modeled using experimental data and mass, momentum and energy conservation constraints. The regimes modeled for spray–film interaction are stick, rebound, spread, and splash. In addition, modified wall functions for evaporating wavy films are provided and tested. The fuel film model is validated through a series of comparisons to experimental data for secondary droplet velocities, secondary droplet sizes, spray radius, spray height, film thickness, film spreading radius, and percentage of fuel adhered to the surface.

Nomenclature

A_{wall} area of the liquid film cell
c_f shear stress coefficient
d_d diameter of drop
f drop impact frequency
h heat transfer coefficient
i_a gas stagnation enthalpy
i_s film stagnation enthalpy
k_s film roughness parameter
L latent heat of vaporization
m_s total mass splashed
M_{tang} tangential velocity source term
M_{vap} rate of fuel vaporization
P_{cell} free-stream pressure
p_d dynamic pressure
P_f heat and mass transfer correlation parameter
Pr_τ turbulent Prandtl number
$\dot{Q}_{imp}$ spray impingement energy source term
$\dot{Q}_{splash}$ splashing droplet energy source term
Re_{k_s} roughness Reynolds number
Sc_τ turbulent Schmidt number
S_d mass source term
$\bar{T}$ mean film temperature
T_B liquid boiling temperature
T_w wall temperature
T_s film interface temperature
u_a gas velocity
u_w wall velocity
$\mathbf{V}_f$ liquid film velocity
y^+ non-dimensional wall distance
y_a fuel vapor mass fraction at y^+
y_s equilibrium vapor mass fraction.

Greek symbols

α spray impingement angle

* Corresponding author. Tel.: 001 608 265 8608; fax: 001 608 262 6707; e-mail: stanton@cae.wisc.edu.

0017-9310/98 $19.00
PII: S0017-9310(98)00054-4

δ liquid film thickness
η_q heat and mass transfer correlation variable
μ kinematic viscosity
σ surface tension
$\bar{\tau}$ average interfacial shear stress
τ_{wall} wall shear
ϕ_i convective velocity parameter
Ψ in-plane angle for rebounding drops
∇_s surface gradient operator.

1. Introduction

The fluid mechanics of drop impingement with surfaces are of importance in a variety of applications. These applications range from agricultural and environmental to nuclear reactor safety, all involving drop and spray impingement on surfaces [1]. As with many phenomena, liquid impact has both negative and positive aspects. The same mechanism that can damage an aircraft can be used to erode and cut materials ranging from plastics, paper, and shoe leather to hard rock [1]. Atmospheric and oceanographic sciences investigate phenomena connected with rain formation and the interaction of rain with the surface of the ocean. Subsequent underwater noise due to rain impingement with the ocean is of great interest to submarine design of sound detection devices, signal processing, and the silencing of vessels [2]. In agriculture, the prevention of soil erosion due to rain plays an important role. Because of its importance, the study of liquid impact has been far-ranging with many interdisciplinary contributions.

Spray–wall interaction is also considered an important phenomenon in internal combustion (IC) engines. The majority of the fuels used in IC engines must be vaporized and mixed with the gas charge in order to combust, expand, and produce power. In an attempt to achieve desirable air–fuel mixing and combustion, the fuels are sprayed in either the carburetor, port, pre-chamber, or directly in-cylinder. In all of these designs, the fuel spray may impinge on engine surfaces before vaporization and mixing are complete. Spray impingement has been shown to influence engine performance and emissions in both compression ignited (CI) and spark ignited engines (SI) [3]. A greater understanding of fuel spray impingement and fuel film formation on engine surfaces is the primary motivation for this research.

Fuel impingement has been shown to affect the emissions and performance in many types of IC engines. Impingement in port injected engines causes difficulties, especially in transient control of the system. A major factor affecting air-fuel ratio during transient operation is the time lag resulting from a film of liquid fuel deposited on the surface of the induction system [3]. This time lag is responsible for decreased engine response, increased fuel consumption, and increased emissions [4]. In port injection engines, a strategy used to decrease the time lag is to spray the fuel on the back of the intake valve to decrease the amount of liquid fuel spread on the walls of the induction system. Yoshikawa [5] performed 3-D modeling of the spray–valve interaction and observed extensive drop interaction between the induction port and intake valve. This interaction is an important source of liquid atomization and vaporization. A better understanding of these interactions between the liquid and induction surfaces will help in designing injection systems and control strategies to improve engine performance and to control emissions.

Spray–wall interactions are also important in direct injection (DI) diesel engines. Several investigators have shown that spray impingement affects engine performance and exhaust emissions [6]. The influence of spray impingement is extremely important in small bore DI engines where the decreased distance between the injector and the piston make impingement more likely. In most small bore engines at high load where the fueling is increased, the spray impingement results in a liquid film formed on the piston and cylinder wall. Under these conditions, fuel impingement is nearly unavoidable and in some cases it is desirable. Werlberger and Cartellieri [7] observed the impinging spray in a small bore (85 mm) direct injection diesel engine and determined that at high loads more than 50 percent of the fuel impinged upon the piston bowl. In computational studies, Gonzalez et al. [8] also found that spray impingement was an important factor in cold start. The smoke levels have been shown to increase during cold start as a result of the accumulation of fuel on the cylinder wall.

The objective of this research is to investigate spray–film impingement, liquid film formation, and post-impingement processes as related to IC engines. More specifically, this work will examine in detail what happens to drops that impinge on solid surfaces that eventually form a liquid fuel film. Also, keeping an account of the fuel film distribution during the mixing and combustion processes is a goal of this work. Consequently, drop impingement on a wetted surface is examined along with post-impingement processes including splashing phenomena. By examining the effects of spray impingement and fuel film formation, this work is incorporated with heat and mass transfer effects in order to complete the formulation and validation of a wall-spray interaction model.

2. Development of thin liquid film model

Based on the droplet impingement work of Naber and Farrell [9] at conditions (e.g., system pressure and temperature) similar to IC engines, a scenario called evaporative wetting would exist which is characterized by the formation of a thin liquid film (10–300 μm). Conse-

quently, spray impingement models should include the possibility of the formation of liquid films on the induction walls and combustion chamber surfaces to accurately model spray–wall phenomena. The liquid film model is based on the physics involved with fuel film flow over 3-D surfaces. The fuel film model simulates thin fuel film flow on solid surfaces of arbitrary configuration.

The continuity, momentum, and energy equations are applied to each wall film cell as shown in Fig. 1(a). By integrating across the film thickness and using 'thin film' assumptions, the equations are reduced to a 2-D film flowing across a 3-D surface.

The major physical processes affecting the liquid film are shown in Fig. 1(b). The physical processes considered include: mass and momentum contributions to the film due to spray impingement, splashing effects, shear forces on the film, piston acceleration, dynamic pressure effects, gravity driven flow, convective heat and mass transfer, and flow separation.

The assumptions used in the formulation of the film model are: the mass flux due to incident drops that impinge is averaged over the wall cell area, lost tangential momentum of impinging drops is added to the film tangential momentum, the velocity profile in the cross-film direction is prescribed to be either laminar or turbulent, and the temperature profile is prescribed to be piecewise linear.

The development of the precursor film is accomplished by averaging the mass of impinging drops that adhere to the wall over the wall cell area. The wall cell is considered to be flooded when the film thickness, δ, is greater than 2 μm. This approach is based on the film thickness measurements of Zhengbai et al. [10].

After integrating in the film normal direction, the continuity equation is transformed into the following form:

$$\frac{\partial \delta}{\partial t} + \frac{1}{A_{\text{wall}}} \sum_{i=1}^{N_{\text{side}}} (\mathbf{V}_f \cdot \hat{n})_i \delta_i l_i = \frac{S_d}{\rho_l A_{\text{wall}}} - \frac{\dot{M}_{\text{vap}}}{\rho_l A_{\text{wall}}} \tag{1}$$

where A_{wall} is the wall area, $\mathbf{V}_f$ is the film velocity, l_i is the length of side i, ρ_l is the film density, δ_i is the film thickness at side i, S_d is a source term, and $\dot{M}_{\text{vap}}$ is the rate of fuel vaporization. The film velocity now has two components located at δ. The source term, S_d, is the mass flux of drops that impinge upon the film or secondary droplets that leave the film which result from splashing. Table 1 contains a summary of the source term for the various impingement regimes as later described in the section on spray–film interaction. The continuity equation for the film thickness resembles the compressible form, because in the 2-D formulation the variation of the film thickness

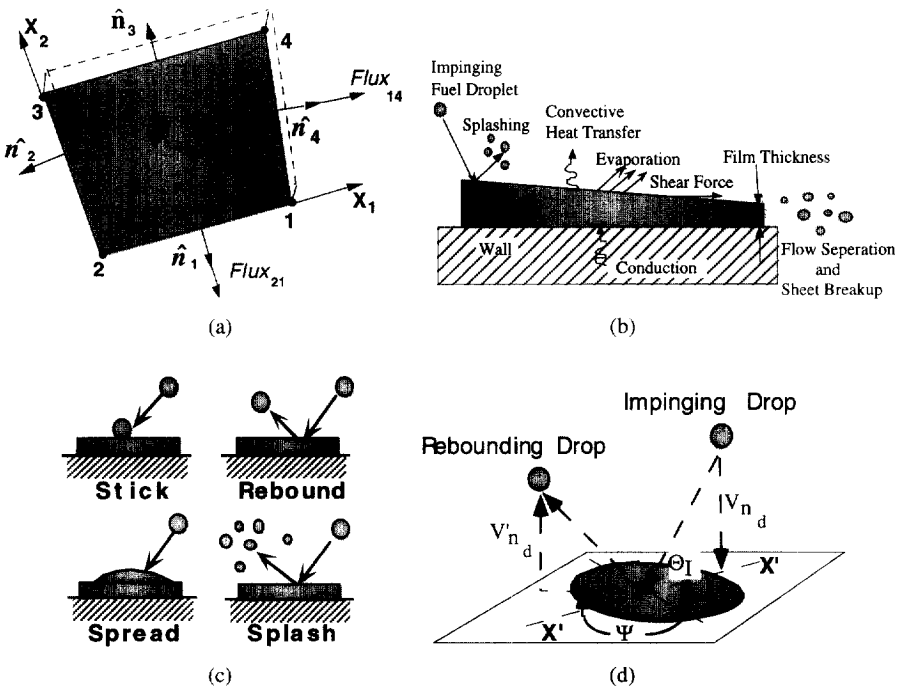

Fig. 1. Schematics of: (a) a typical wall film cell used in the formulation of the film model; (b) the major physical phenomena governing film flow; (c) the various impingement regimes identified in the spray–film interaction model; and (d) Velocity of a rebounding drop from a thin liquid film.

Table 1
A summary of the source term for the various impingement regimes identified in the spray–film interaction model [see equations (1) and (2)]

Impingement regime	Source term S_d	Nomenclature
Stick	$\frac{\pi}{6}\rho_l \sum_{k=1}^{N_{drop}} (N_k d_{d_k}^3)$	d_{d_k}—diameter of incident drop N_{drop}—number of incident drops or parcels N_k—number of particles in the incident parcel
Rebound	0	—
Spread	$\frac{\pi}{6}\rho_l \sum_{k=1}^{N_{drop}} (N_k d_{d_k}^3)$	Similar to stick
Splash	$\frac{\pi}{6}\rho_l \sum_{k=1}^{N_{drop}} \left[1-\left(\frac{m_s}{m_d}\right)_k\right] N_k d_{d_k}^3$	$(m_s/m_d)_k$—mass fraction splashed
	Dynamic pressure, p_d	
Stick	$\rho_l \sum_{k=1}^{N_{drop}} V_{n_{d_k}}^2 \frac{A_{d_k}}{A_{wall}}$	$V_{n_{d_k}}$—normal velocity component of incident drop N_{drop}—number of incident drops or parcels
Rebound	$\rho_l \sum_{k=1}^{N_{drop}} (1+e_k^2) V_{n_{d_k}}^2$	e_k—coefficient of restitution for the k-th drop
Spread	$\rho_l \sum_{k=1}^{N_{drop}} V_{n_{d_k}}^2 \frac{A_{d_k}}{A_{wall}}$	Similar to stick
Splash	$\rho_l \sum_{k=1}^{N_{drop}} V_{n_{d_k}}^2 + \rho_l \sum_{j=1}^{N_{splash}} V_{nj}^2$	V_{nj}—normal velocity component of the j-th secondary droplet N_{splash}—number of secondary droplets
	Tangential momentum, M_{tang}	
Stick	$\frac{\pi}{6}\rho_l \sum_{k=1}^{N_{drop}} (N_k d_{d_k}^3 V_{\tau_{dk}})$	$V_{\tau_{dk}}$—tangential velocity component of incident drop N_{drop}—number of incident drops of parcels N_k—number of particles in the incident parcel
Rebound	$\frac{\pi}{6}\rho_l \sum_{k=1}^{N_{drop}} N_k d_{d_k}^3 \left(\frac{2}{7} V_{\tau_{dk}}\right)$	—
Spread	$\frac{\pi}{6}\rho_l \sum_{k=1}^{N_{drop}} (N_k d_{d_k}^3 V_{\tau_{dk}})$	Similar to stick
Splash	$\frac{\pi}{6}\rho_l \sum_{k=1}^{N_{drop}} (N_k d_{d_k}^3 V_{\tau_{dk}}) + \frac{\pi}{6}\rho_l \sum_{j=1}^{N_{splash}} (N_j d_j^3 V_{\tau j})$	$V_{\tau j}$—tangential velocity component of j-th secondary droplet N_{splash}—number of secondary droplets or parcel N_j—number of particles in the j-th parcel resulting from splashing

is mathematically analogous to a virtual compressibility. In a similar fashion, the momentum equation is transformed into the following form:

$$\frac{\partial(\delta \mathbf{V}_f)}{\partial t} + \frac{1}{A_{wall}} \sum_{i=1}^{N_{side}} \mathbf{V}_f (\mathbf{V}_f \cdot \hat{n})_i \delta_i l_i \phi_i = -\frac{\sum_{i=1}^{N_{side}} (P\hat{n})\delta_i l_i}{\rho_l A_{wall}} + \mathbf{g}\delta + \frac{M_{tang}}{\rho_l A_{wall}} + \frac{\sum_{i=1}^{N_{edge}} (\tau A_i)}{\rho_l A_{wall}} + \mathbf{a}\delta. \quad (2)$$

The first term is the time derivative of the film momentum per unit area. The second term in equation (2) is the

convective momentum term and is approximated using equations (3) and (4):

$$\int_{L_1}^{L_2}\int_0^{\delta}\mathbf{V}_f(\mathbf{V}_f\cdot\hat{n})\,\mathrm{d}\hat{x}_3\,\mathrm{d}\hat{x}_1 \approx \sum_{i=1}^{N_{\text{side}}}\mathbf{V}_f(\mathbf{V}_f\cdot\hat{n})_i\delta_i l_i\phi_i \tag{3}$$

with

$$\phi = \frac{1}{1-\dfrac{\delta_i}{\delta}} - \frac{\Theta_i}{\delta}\frac{1}{\left(1-\dfrac{\delta_i}{\delta}\right)^2}. \tag{4}$$

Equation (4) results from the approximation of the integration of the non-linear convective term in the cross-film direction. The displacement thickness, δ_i, and the momentum thickness, Θ_i, in equation (4) can be calculated once the velocity profile in the cross-film direction has been chosen.

The third term in equation (2) is the pressure term and is described by equation (5) which includes the dynamic pressure term, p_d, which results from incident drop impingement and splashing effects:

$$P = P_{\text{cell}} + p_d \tag{5}$$

P_{cell} is the free-stream pressure (i.e., gas pressure). Table 1 contains a summary of the dynamic pressure term for the various spray-film impingement regimes. The velocity, $\mathbf{V}_{n_d}$, is the normal component of velocity of the incident drop and V_{n_i} is the normal component of velocity of the i-th secondary droplet resulting from splashing. N_{drop} and N_{splash} are the total number of incident drops and the total number of splashed droplets, respectively. The area, A_{d_k}, is the area of the k-th incident drop while A_j is the area of the j-th secondary drop. The pressure is assumed not to vary in the cross-film direction due to the 'thin film' assumption. The dynamic pressure term is also assumed constant normal to the wall.

The fourth term in equation (2) captures the gravity effect of the liquid film flow. This effect is important in film flow along inclined or vertical surfaces.

The fifth term in equation (2) is the tangential momentum contribution to the film as a result of spray impingement and splashing of secondary droplets. This term is calculated using equation (6):

$$M_{\text{tang}} = \sum_{i=1}^{N_{\text{drop}}}(m_i\mathbf{V}_{\tau_{d_i}}) - \sum_{j=1}^{N_{\text{splash}}}(m_j\mathbf{V}\tau_j). \tag{6}$$

The first term on the right side of equation (6) is the momentum contribution of the incident drops, while the second term on the right side is the momentum contribution due to the secondary droplets. Table 1 contains a summary of the tangential momentum contribution for the spray–film impingement regimes.

The sixth term in equation (2) is the viscous film term and is calculated using equations (7):

$$\sum_{i=1}^{N_{\text{side}}}(\tau_i A_i) = \tau_{\text{wall}}A_{\text{wall}} + \bar{\tau}A_{\text{wall}} \tag{7}$$

where τ_{wall} is the wall shear and $\bar{\tau}$ is the shear at the liquid–gas interface. The wall shear is calculated using equation (8) once the velocity profile in the cross-film direction is chosen:

$$\tau_{\text{wall}} = \mu\left.\frac{\partial\mathbf{V}_f}{\partial\hat{x}_3}\right|_{\hat{x}_3=0}. \tag{8}$$

The viscous shear at the liquid–gas interface is calculated using wall functions for a wavy, evaporating film as described in the following section on modified wall functions. Finally, the seventh term in equation (2) is due to the piston acceleration, **a**. Note, the source terms S_d, p_d, and M_{tang} as described in Table 1 have been modified to include the effect of moving surfaces but are excluded for brevity.

In keeping with the 2-D film formulation, the energy equation is used to calculate the mean film temperature, $\bar{T}$, by assuming a piecewise linear temperature profile. In a similar manner as [11], the profile varies from the wall temperature T_w, to T_f in the lower half of the film and from T_f to an interface temperature, T_s, in the upper half of the film. Thus, after assuming a linear velocity profile and integrating in the direction normal to the wall, the film energy equation is

$$\rho c_l\frac{\partial(\bar{T}\delta)}{\partial t} + [\mathbf{V}_f\cdot\nabla_s]\left[\bar{T}+\frac{T_s-T_w}{6}\right] = k\left[\frac{T_s-\bar{T}}{\delta/4}-\frac{\bar{T}-T_w}{\delta/4}\right]+\dot{Q}_{\text{imp}}-\dot{Q}_{\text{splash}} \tag{9}$$

where c_l is the liquid specific heat (temperature dependent), k is the liquid film thermal conductivity (temperature dependent), ∇_s is the surface gradient operator, $\dot{Q}_{\text{imp}}$ is an energy source term due to the impinging spray, and $\dot{Q}_{\text{splash}}$ is an energy source term due to droplets that splash.

An interface conservation condition relating the convective heat transfer, $\dot{Q}$, to the film, the energy used to vaporize fuel, and the liquid thermal conduction is needed to calculate the interface temperature T_s:

$$\dot{Q} = k\frac{T_s-[2\bar{T}-(T_w+T_s)/2]}{\delta/2} + \dot{M}_{\text{vap}}L = h(T_\infty - T_s) \tag{10}$$

where L is the latent heat of vaporization, $\dot{M}_{\text{vap}}$ is the rate of fuel vaporization and h is the heat transfer coefficient for the film. The expressions used for h and $\dot{M}_{\text{vap}}$ will be given later by the modified wall functions. However, if the gas velocity is zero near the wall, the interface conservation equation becomes

$$\dot{Q} = k\frac{T_s-[2\bar{T}-(T_w+T_s)/2]}{\delta/2} + \dot{M}_{\text{vap}}L = \frac{k(T_\infty - T_s)}{\delta_l/2} \tag{11}$$

where δ_l is a representative distance from the film surface to the free stream.

The liquid film continuity and momentum equations (1) and (2) are numerically solved using a predictor-corrector scheme. The predictor-corrector scheme consists of using the Euler method as a predictor followed by the trapezoid rule as a corrector. However, the mean film temperature and film interface temperature, given by equations (9) and (10), are solved implicitly using a damped Newton iteration scheme.

3. Modified wall functions

In order to complete the calculation method for film heat and mass transfer, a heat transfer coefficient h and a mass transfer rate $\dot{M}_{vap}$ must be determined from wall functions for vaporizing films. Vaporization alters the structure of the gas phase turbulent boundary layers above the wall films because of the existence of gas velocities normal to the wall induced by the vaporization.

Himmelbauch et al. [12] proposed a series of wall functions for evaporating, wavy films in which satisfactory results were obtained for airblast atomizers. A similar approach has been adopted with modifications for dense sprays. Additional validation for the modified wall functions can be found for condensing and evaporating falling films [13, 14].

The boundary conditions near the phase interface are described by a film roughness approach proposed by Sattelmyer and Wittig [15]:

$$k_s = 2\Phi\delta$$
$$\Phi = 0.735 + 0.009255\bar{\tau} \tag{12}$$

where k_s is the film roughness and $\bar{\tau}$ is an average shear stress. The latter is calculated using equation (13) which accounts for pressure gradients and mass flow normal to the film surface:

$$\bar{\tau} = \tau_w + \frac{\dot{M}''_{vap} u_a}{\left[1 + \frac{[\tau_w/(\rho_a u_a)]^{0.5}}{\kappa}\right]} + 0.5\delta\frac{dp}{dx} \tag{13}$$

where u_a is the gas velocity at the non-dimensional normal coordinate:

$$y^+ = \frac{yC_\mu^{0.25}K^{0.5}}{v_l} \quad \text{where } K = \frac{\bar{\tau}/\rho_a}{C_\mu^{0.5}}. \tag{14}$$

This film roughness influences the air flow by altering the C constant in the logarithmic law of the wall as shown in equation (15) below:

$$u^+ = \frac{1}{\kappa}\ln(y^+) + C. \tag{15}$$

The constant C is a function of the roughness Reynolds number which is defined as

$$Re_{k_s} = \frac{k_s u_\tau}{v}. \tag{16}$$

For the C function, three sections are distinguished by

$$C = 5.15 \qquad Re_{k_s} < 5$$
$$C = 1.5497 + 19.1\log(Re_{k_s}) - 14.43[\log(Re_{k_s})]^2 + 3.31[\log(Re_{k_s})]^3 - \frac{1}{\kappa}\ln(Re_{k_s}) \qquad 5 \leqslant Re_{k_s} \leqslant 70$$
$$C = 8.5 - \frac{1}{\kappa}\ln(Re_{k_s}) \qquad 70 < Re_{k_s}. \tag{17}$$

Thus, combining equations (13), (14) and (15) and evaluating at $y = \delta$, the shear stress at the film interface is given by

$$\frac{u_a\rho_a C_\mu^{0.25}K^{0.5}}{\bar{\tau}} = \frac{1}{\kappa}\ln\left(\frac{\delta C_\mu^{0.25}K^{0.5}}{v_a}\right) + Cy^+ > y_c^+$$
$$\frac{u_a\rho_a C_\mu^{0.25}K^{0.5}}{\bar{\tau}} = y^+ \qquad y^+ < y_c^+. \tag{18}$$

Note that the value of y_c^+ is determined to give a continuous transition between the turbulent and laminar regions by iteratively solving for y_c^+ using

$$y_c^+ = \frac{1}{\kappa}\ln(y_c^+) + C. \tag{19}$$

Also, the relative velocity $|u_{a_t} - u_w|$ is used in the wall functions for fuel films on moving surfaces where u_w is the wall velocity and u_{a_t} is the film velocity tangent to the wall.

For the prediction of the heat and mass transfer processes, the standard wall functions for the stagnation temperature and the vapor concentration are used [15]. However, experiments of Sill [16] show that the roughness of the wavy liquid film has a lesser effect on the heat and mass transfer in comparison to the momentum transfer. Therefore, an empirical correlation is given by Sill [16], relating the enhancement of heat transfer by roughened surfaces by

$$\eta_q = \log\left(\frac{Pr^{0.33}}{Re_{k_s}^{0.243}}\right) - 0.32\times10^{-3}\,Re_{k_s}\log(Pr) + 1.225. \tag{20}$$

Thus, the wall function for the heat transfer with evaporating wavy film surfaces is

$$\frac{-\dot{Q}}{\rho_a u_a\left[i_a - i_s - (1 - Pr_\tau)\frac{u_a^2}{2}\right]} = \frac{\eta_q c_f}{Pr_\tau(1 + P_f\sqrt{\eta_q c_f})} \tag{21}$$

where i_a is the stagnation enthalpy of the gas flow, i_s is the stagnation enthalpy of the film at the interface temperature of T_s, and Pr_τ is the turbulent Prandtl

number. The variables c_f and P_f are given by equations (22) and (23), respectively:

$$c_f = \frac{\bar{\tau}}{\rho_a u_a^2} \tag{22}$$

$$P_f = 9.0\left(\frac{Pr}{Pr_\tau} - 1\right)\left(\frac{Pr_\tau}{Pr}\right)^{0.25}. \tag{23}$$

The corresponding wall function for the mass transfer is obtained from the assumption that the effect of roughness on the mass transfer can be described in similarity to the heat transfer by replacing the Prandtl numbers by the Schmidt numbers:

$$\frac{-\dot{M}''_{\text{vap}}(1-y_s)}{\rho_a u_a (y_a - y_s)} = \frac{\eta_m c_f}{Sc_\tau(1 + P_f\sqrt{\eta_m c_f})} \tag{24}$$

where y_s is the equilibrium vapor mass fraction at the film surface temperature, y_a is the fuel vapor mass fraction at y^+, Sc_τ is the turbulent Schmidt number, and η_m is given by equation (20) with Sc replacing Pr.

4. Development of spray–wall interaction model

Many different scenarios of drop impact can be distinguished according to the circumstances under which the impact happens. The outcome of a collision depends on the properties of the drop, of the impact surface, and of the fluid which the drop traverses before impact. The surface impacted can be either solid or liquid. In the latter case, the solid surface is covered by a thin, liquid film. In IC engine spray impingement, a collection of drops impinge onto the wetted surface simultaneously or successively with the likelihood that each impinging drop will feel the effects of its neighboring drops. This process is extremely complex and knowledge of the process remains limited. Nevertheless, information on multi-drop impingement (i.e., a train of drops with a known frequency) exists that is useful in formulating the spray–film interaction model.

In general, the impingement regimes are determined by the parameters describing the arriving drops, the wall surface conditions and (if present) the gas boundary layer characteristics in the near-wall region. Of particular interest in identifying impingement regimes is the wall temperature relative to the following temperatures:

$$T_B < T_{pa} < T_N < T_{pr} < T_{\text{Leid}} \tag{25}$$

where T_B is the liquid boiling temperature, T_{pa} is the pure adhesion temperature below which drop adhesion occurs at low impact energy, T_N is the Nakayama temperature at which a drop reaches its maximum evaporation rate, T_{pr} is the pure rebound temperature above which bounce occurs at low impact energy, and T_{Leid} is the Leidenfrost temperature. The collision of a drop with a liquid surface, where the wall temperature (T_w) is less than the liquid boiling temperature (T_B) as encountered in most IC engine applications, may result in sticking, bouncing, spreading, or splashing [1, 17]. The various impingement regimes are shown in Fig. 1(c). The details of the spray–film interaction model have been described previously in the literature [13, 14, 18] and are only briefly summarized.

The stick regime occurs when an impinging drop adheres to the film surface in nearly a spherical form. This often happens when the impact energy is extremely low, and the wall temperature is below the pure adhesion temperature, T_{pa}. The transition criteria for the stick regime is $We < 5$. This criteria is based on the experimental results of various investigations [19, 20]. In this spray–film model, a drop that is in this regime is assumed to coalesce completely with the liquid film.

Next, the rebound regime occurs when the impinging drop bounces off the film when the impact energy is low. The air layer trapped between the drop and the liquid film causes low energy loss resulting in bouncing. The transition criteria for the rebounding regime is $5 < We < 10$. This criteria is based on the experimental work of Rodriguez and Mesler [19] and Stow and Hadfield [21]. In this regime, the rebound drop velocity magnitude and direction need to be determined. The velocity of the rebounding drop is determined using equations developed by Matsumoto and Saito [22] for small particles bouncing on a wetted surface. The in-plane angle, Ψ, is measured from the x' axis as shown in Fig. 1(d). The variation in Ψ is calculated using equation (26) and equation (27) which were developed by considering mass and momentum conservation of an impinging liquid jet [13, 23]:

$$\Psi = -\frac{\pi}{\beta}\ln\left[1 - p(1 - e^{-\beta})\right] \tag{26}$$

where p is a random number uniform on the interval (0, 1) while β is given by

$$\sin\alpha = \left[\frac{e^{\beta}+1}{e^{\beta}-1}\right]\frac{1}{1+(\pi/\beta)^2} \tag{27}$$

with α being the wall inclination angle.

The rebound characteristics of the model are consistent with experimental observations of Stow and Stainer [24] and Levin and Hobbs [25] for drop impingement on rough surfaces. These investigators reported little difference between drop impact with a thin liquid film (10–300 μm) and that of a rough surface. The lost momentum of the rebounding drop contributes to the momentum balance of the liquid film as previously described.

The third regime, spreading, is similar to the sticking regime but occurs at higher We. In this regime, the drop merges with the liquid film upon impact. The transition criteria for spreading is

$$10 < We < 18.0^2 d_d \left(\frac{\rho}{\sigma}\right)^{1.2} v^{1.4} f^{3.4} \tag{28}$$

where ρ, σ, v, and f are the drop density, surface tension, kinematic viscosity, and frequency of the impinging drops. The last term, containing f, in equation (28), is known as the splashing threshold for the multi-drop impact with a thin liquid film as reported by Yarin and Weiss [26].

The final regime is splashing and occurs at high impact energy. Upon impact, a crater is formed with a crown at the periphery where liquid jets become unstable and break up into many secondary droplets. In this regime, many quantities need to be calculated in order to describe the process. These quantities include the proportion of incident drop mass deposited as part of the liquid film and the sizes, number, velocities, and ejection angles of secondary droplets. The formulation of these splashing quantities is based on the experimental work of Mundo et al. [27] and Yarin and Weiss [26] along with mass, momentum, and energy conservation constraints. Mundo et al. [27] investigated multi-drop impingement on rough surfaces, while Yarin and Weiss [26] investigated multi-drop impingement on thin liquid films.

The transition criteria for the splashing regime is given by the following expression:

$$18.0^2 d_d \left(\frac{\rho}{\sigma}\right)^{1/2} v^{1/4} f^{3/4} < We. \tag{29}$$

The splashing threshold corresponds to developed crown instability, strong enough to produce a cloud of secondary droplets. In some cases below this threshold, a crown is not high enough or the process is not long enough to produce secondary droplets. Therefore, crown formation begins slightly below the splashing threshold. In order to calculate the splashing threshold, the drop frequency, f, needs to be determined. This is accomplished by calculating f for each impinging drop, regardless of its associated impingement regime. By calculating the frequency and using expression (29), each impinging drop can be tested for the onset of splashing. The frequency is calculated as the inverse of the time between drop impacts. The frequency for the first drop to impact the film is ambiguous so it is calculated by $f = V_{n_d}/d_d$ where V_{n_d} and d_d are the drop normal component of velocity and drop diameter, respectively.

5. The computer code

The thin liquid film and spray-wall interaction models were implemented into a modified version of the KIVA-II computer code, originally developed at Los Alamos National Lab [28]. KIVA-II solves unsteady, compressible, turbulent-reacting flows on finite-volume grids, together with the dynamics of an evaporating liquid spray. With the addition and modification of many submodels, the code has been widely applied and validated for engine combustion simulations [29].

The conservation laws for gas mass, momentum, internal energy and scalar turbulence variables (RNG k–ε model) are solved in KIVA-II subject to the appropriate initial and boundary conditions using a time-marching explicit numerical method. Stochastic parcel injection is used for the spray drops. In this technique, each computational parcel represents a number or group of physically similar drops (i.e., similar kinematic and thermodynamic properties). The drop parcels exchange mass, momentum and energy with the gas through source terms in the gas equations.

Of particular interest to this work, the wave breakup model has been adopted to simulate the atomization process of the free spray [30]. The spray breakup model also considers the effect of drop distortion on the drag coefficient of the drops, as well as droplet–droplet interaction with the possibility of coalescence [30].

Finally, the effects of the thin liquid film on the gas equations solved by KIVA-II is through wall source terms S_p, S_u, and S_i:

$$S_p = \dot{M}_{\text{vap}} \delta^*(y - y_s) \tag{30}$$

$$S_u = [\dot{M}_{\text{vap}}(\mathbf{V}_f - \bar{u}_w) - \bar{\tau}]\delta^*(y - y_s) \tag{31}$$

and

$$S_i = [\dot{M}_{\text{vap}} L - \dot{Q}]\delta^*(y - y_s) \tag{32}$$

where y is the coordinate normal to the wall surface, y_s is the value of y at the gas–liquid interface, δ^* is the delta function, $\dot{M}_{\text{vap}}$ is the rate of vaporization [see equation (24)], $\dot{Q}$ is the convective heat transfer [see equation (21)], $\bar{\tau}$ is the interfacial shear stress [see equation (13)], $\mathbf{V}_f$ is the fuel film velocity, and $\bar{u}_w$ is the wall velocity.

6. Results and discussion

To validate the spray-film interaction model and the liquid film model, KIVA-II is used to simulate various experiments involving fuel injectors. The long-range goal is to examine spray-wall interaction inside the engine cylinder under realistic operating conditions. However, this requires many intermediate steps in which the models are validated under atmospheric pressures and wall temperature conditions, as well as high pressure and high wall temperature environments without combustion. In addition, the models have been used for a variety of engine simulations [13, 14], in which the film model provides a predictive tool for the examination of wall wetting and secondary atomization characteristics at varying engine loads.

However, for this study the aim is to focus on the transient behavior of the two-phase wall-jet resulting from spray impingement on a wall with the eventual formation of a thin liquid film. The numerical results are

compared to well characterized experimental data for spray radius, spray height, liquid film thickness, liquid film spreading radius, percentage of fuel adhered to the surface, secondary droplet velocities, and secondary droplet size.

7. Spray dynamics and film spreading

The liquid film spreading characteristics and spatial and temporal behavior of an impinging spray were investigated by Saito et al. [31] using high speed photography. The investigation involved injection in a pressurized chamber under conditions closely approximating those found in a diesel engine. A summary of the experimental conditions are shown in Table 2 (as indicated by case 1 in column 2).

Two different injection pressures were considered: 30 and 120 MPa, with an impingement angle of 90 . Figure 2(a) and (b) show the results for the spray radius and spray height for both injection pressures. The spray radius is the distance as measured from the centerline of the spray while the spray height is the distance as measured normal to the surface. For these comparisons, the computed spray radius is defined as the radius of a cylindrical body which contains 98 percent of the total spray. In a similar manner, the spray height is defined as the normal distance from the wall to the droplet parcel above which less than 2 percent of the post-impinged droplets lie. The agreement is good for both injection cases in which the computed results capture the trend that the higher injection pressure leads to larger spray radius and height. Based on the results of the simulations, these trends can be attributed to the larger normal velocities of the secondary droplets due to intense splashing associated with the higher injection pressure. Moreover, the secondary droplets in the wall spray generally possess larger tangential velocities due to the increased gas velocities.

Comparisons of the liquid film spreading radius and mean film thickness are shown in Fig. 2(c) and (d), respectively. The mean film thickness is defined as the total film volume divided by the surface area covered by the film. The computed results provide good agreement for both pressure conditions. The predictions show that for the higher injection pressure the film spreads faster while the thickness becomes thinner. The higher injection pressure leads to increased droplet and gas impingement velocities which promote faster film spreading. These effects are accounted for in the model through the dynamic pressure (p_d) and the droplet tangential momentum source term (M_{tang}) [see equation (2)]. Additionally, the higher injection pressure results in less mass deposited (or adhered) on the wall as shown in Fig. 2(e). These trends serve to explain the mean film thickness behavior.

Also included in Fig. 2(c) is a test case of the static film spreading radius for the 120 MPa injection pressure. The static film spreading behavior was determined by omitting the film momentum equation (2) in the simulation. This test shows that considerable discrepancies occur in the results when the kinematic behavior of the film is neglected.

In the experimental study of adhered fuel on the wall, the angle of impingement was varied with the results shown in Fig. 2(e). The computed results provide good agreement for the majority of the impingement angles with the largest discrepancy occurring for the 60 impingement angle at 120 MPa. The predictions capture the trend that less fuel adheres to the wall for the higher injection pressure for all impingement angles considered. Based on the simulations, higher injection pressure leads to increased free spray atomization resulting in smaller impinging drops. Occasionally, more small drops are carried away by the gas phase wall vortex structure in the

Table 2
Specification of test conditions for Saito et al. and Arcoumanis and Chang impingement simulations

	Case 1: Saito et al.	Case 2: Arcoumanis and Chang
Wall distance (mm)	25	30
Wall temperature (K)	293	293 and 423
Gas temperature (K)	293	293
Gas pressure (bar)	21	1
Nozzle diameter (mm)	0.25	0.22
Injection angle ( )	45, 60, 75, 90	90
Injection duration (ms)	2.85 and 1.425	1.0
Fuel injected (mm^3 $pulse^{-1}$)	35	4.0
Injection pressure (MPa)	30 and 120	26
Fuel	Diesel no. 2	Diesel no. 2
Liquid density (g cm^{-3})	0.720	0.825
Ambient gas	N_2	Air

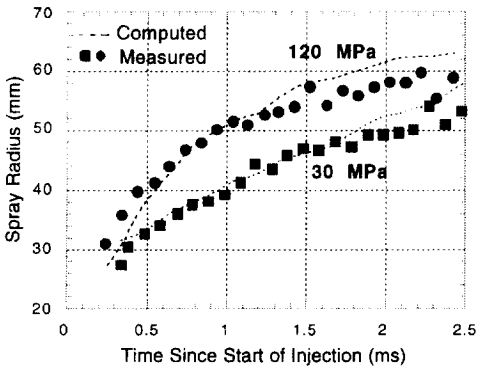

(a)

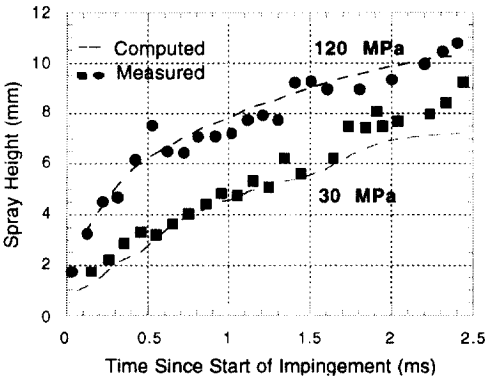

(b)

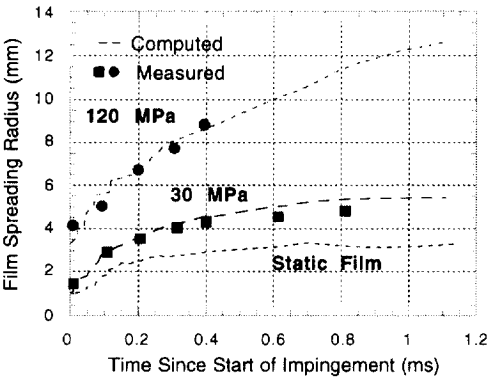

(c)

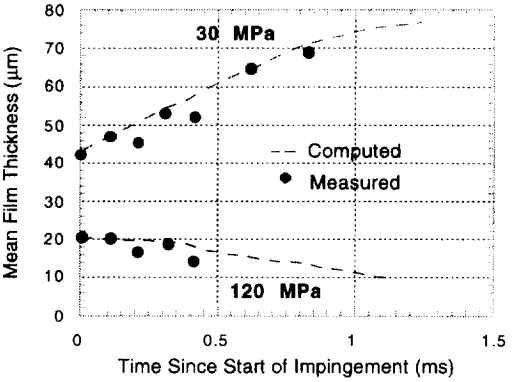

(d)

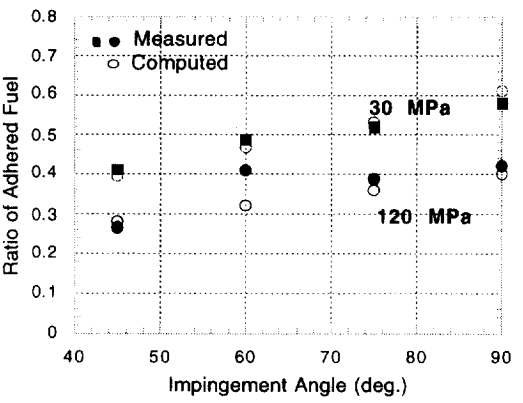

(e)

Fig. 2. Flat plate impingement comparison for (a) spray radius, (b) spray height, (c) film spreading radius and (d) mean film thickness with a 90° impingement angle, while (e) shows a comparison of the quantity of impinging mass adhered to the surface of a flat plate for varying impingement angles.

near-wall region before impingement occurs.* This behavior leads to less adhered fuel. In a similar fashion, the higher pressure leads to more energetic impacts resulting in a larger number of splashed droplets which in turn become entrained in the wall vortex structure.

8. Spray impingement drop sizes and velocities

The spatial and temporal characteristics of transient diesel sprays impinging at 90° on unheated and heated walls were investigated by Arcoumanis and Chang [32] using phase Doppler anemometry. Their work provides evidence concerning the effects that the presence of the flat wall exerts on the droplet size and tangential velocity of the spray. The detailed information about the droplet dynamics in the vicinity of a wall is required to characterize the spray-wall interaction and its effect on secondary atomization and fuel/air mixing as well as the structure of the developing liquid wall-jet. A summary of the test conditions used in this investigation is shown in Table 2 (as indicated by case 2 in column 3). Additional information on the injector and distributor-type fuel injection pump can be found in Arcoumanis and Chang [33].

Comparisons are performed along the wall at radial distances of 6, 10 and 15 mm from the incident spray axis and at two locations away from the wall of 0.5 and 3.0 mm (see Fig. 3). These measuring locations correspond to representative regions of the two-phase wall-jet as shown in Fig. 3 which include: the main wall-jet region, the stagnation region and the downstream region. All the measurement positions were located outside the spray impingement area to ensure that droplets associated with the incident free spray were not considered in the analysis of the wall-jet. A total of 2000 spray parcels were used in the simulation which utilizes a 60° sector mesh. The large number of parcels in the simulations were needed to ensure an adequate number of particles to provide representative statistical information describing the wall spray event. Each measurement point consisted of an ensemble of approximately 2500 data (or particles) that were collected within a 50 μs time interval. This procedure was particularly important in describing the spray impingement data at the onset of impingement at the 6 mm radial location.

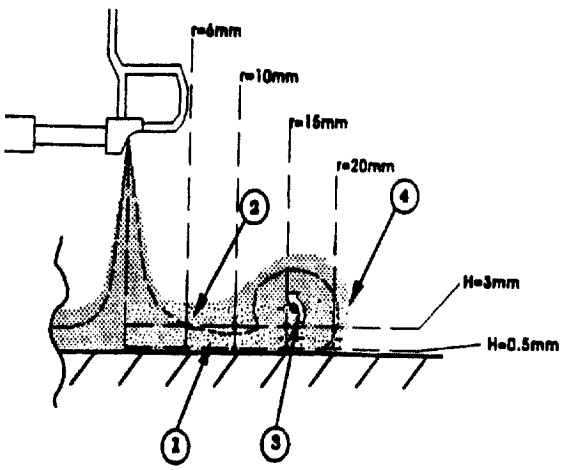

Fig. 3. PDA measurement locations within the two-phase wall-jet following impingement of the spray on the flat plate with the following structures: (1) main wall-jet region; (2) stagnation region; (3) wall-jet vortex; and (4) leading edge [39].

Representative spray images are shown in Fig. 4(a)–(f) for a wall temperature (T_w) of 150°C. The small drop sizes near the wall result from secondary atomization due to splashing. The gas velocity profiles reveal a wall-jet emanating radially outward from the spray impingement region, near the tip of which there is a vortex. This vortex is progressively radially stretched at later times (see Fig. 4(b), (d) and (f)). It is this vortex structure which influences the movement of drops, especially the smaller secondary droplets that result from splashing. Consequently, drops have the opportunity to coalesce and form larger drops. Also, film thickness profiles are shown in Fig. 4(g) and (h) for the two wall temperatures. The film is thicker for the low temperature wall (Fig. 9(g)) due to less fuel vaporization and higher liquid viscosity. This thicker film also influences the secondary atomization as will be discussed later in this section.

The temporal behavior of the tangential velocities are compared in Fig. 5. Figure 5 contains results obtained at a height of 0.5 mm from the wall and a radial distance of 6, 10 and 15 mm for T_w = 20°C and radial distances of 6 and 10 mm for T_w = 150°C. Also shown in the figures are vertical lines indicating the approximate time the wall vortex moves through the measurement location. Additional analysis of the wall vortex is given in subsequent parts of this section. For the tangential velocity profiles near the wall, the predicted results show similar trends as the experimental data for both wall temperatures. As the radial distance increases, the maximum tangential velocity decreases as the liquid wall-jet is decelerated. However, the tangential velocities are greatest in the high wall temperature case. This may be attributed to the interaction of turbulent air flow resulting from enhanced air entrainment as the wall vortex moves radially with a higher convective velocity (see later discussion for Fig. 9).

Figure 6(a)–(c) are results obtained at a height of 3.0 mm from the wall and at radial distances of 6, 10 and 15 mm, respectively, for T_w = 20°C, while Fig. 6(d) and (e)

* More details of a typical gas phase wall vortex are studied in the next section.

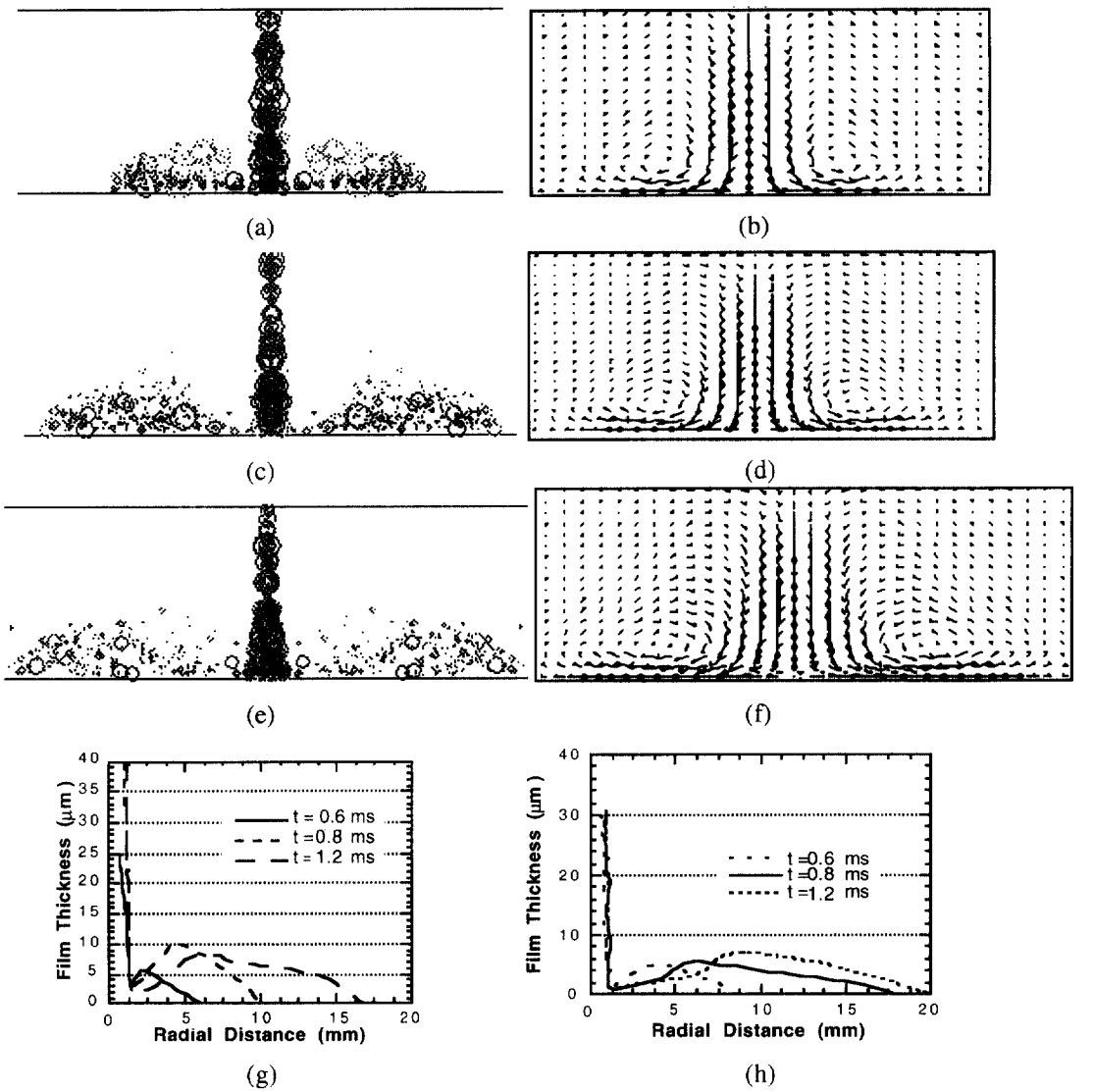

Fig. 4. Results for the simulation of the Arcoumanis and Chang experiment for $T_w = 150°C$ with (a) spray image at 0.6 ms, (b) velocity profile at 0.6 ms, (c) spray image at 0.8 ms, (d) velocity profile at 0.8 ms, (e) spray image at 1.2 ms and (f) velocity profile at 1.2 ms. Also shown are liquid film thickness profiles at various times for (g) $T_w = 20°C$ and (h) $T_w = 150°C$.

are results at the same height but at radial distances of 6 and 10 mm for $T_w = 150°C$. The discrepancies are greater at the locations corresponding to the spray stagnation region (see Fig. 3) for $T_w = 20°C$. However, good agreement is obtained for the high wall temperature case. The affect of wall temperature on the tangential velocity becomes less noticeable farther from the wall. Comparing Fig. 5 and Fig. 6, the results show that the maximum velocity is observed at the distance nearest the wall ($h = 0.5$ mm). The agreement is good for the curves at a radial distance of 6 mm (see Fig. 6(a)) except at the latter stage of injection. The tangential velocity starts at a maximum velocity and then decays to approximately zero before increasing again. At a radial distance of 10 mm (see Fig. 6(b) and (e)), all curves exhibit a change in slope as soon as the leading edge of the wall-jet reaches the measurement location as indicated by the vertical lines. This suggests the existence of a wall vortex structure moving across the control volume.

By comparing Fig. 6(b) and (e), the magnitude of the change in tangential velocities at approximately 1.0 ms is greater for the high wall temperature case. This behavior helps explain the existence of a stronger head vortex moving radially across the wall. The behavior also exists

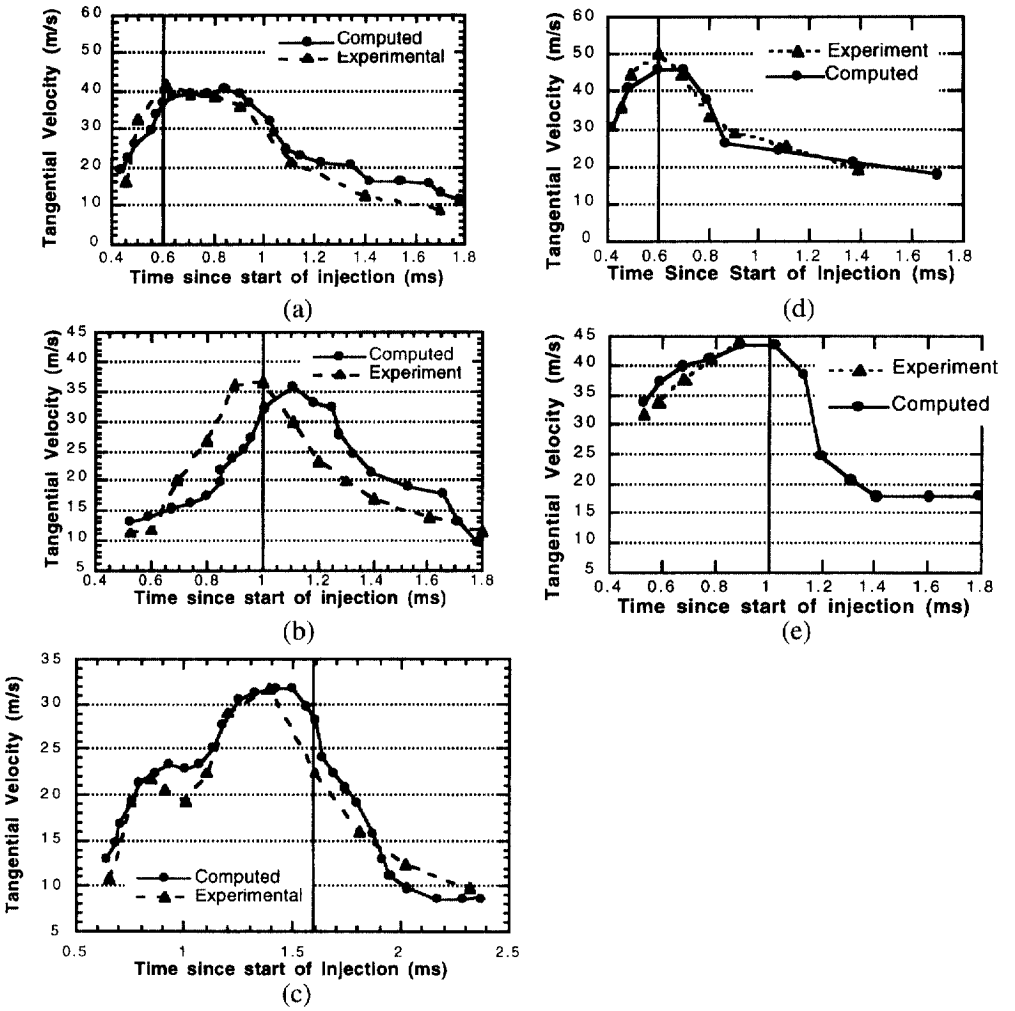

Fig. 5. Temporal history of the droplet tangential velocity at a height of 0.5 mm from the wall surface and at a radial distance of (a) 6 mm and $T_w = 20°C$, (b) 10 mm and $T_w = 20°C$, (c) 15 mm and $T_w = 20°C$, (d) 6 mm and $T_w = 150°C$, and (e) 10 mm and $T_w = 150°C$.

at a radial distance of 15 mm as indicated by the curves in Fig. 6(c). The peak values of the tangential velocity of the droplets become smaller due to the loss of momentum of the droplets with increasing radial distance. By comparing the tangential velocities at different heights (0.5 and 3.0 mm), it becomes apparent that most of the droplet tangential velocity remains concentrated in the region near the wall surface during the main injection period.

Figure 7(a)–(c) are results obtained for the sauter mean diameter (SMD) of the droplets at a height of 0.5 mm from the wall and at radial distances of 6, 10 and 15 mm, respectively, for $T_w = 20°C$, while Fig. 7(d) and (e) are for the same height and radial distances of 6 and 10 mm for $T_w = 150°C$. Figure 8 shows corresponding results at a height of 3.0 mm from the wall. No clear trends are evident between the high temperature and low temperature cases. The computed results provide quantitative estimates of SMD. In most cases, the computed results provide similar trends through the majority of the impingement event. Some discrepancies between experiments and computations are apparent for all radial distances especially at the latter stages of injection. During the early injection period, the SMD values for $T_w = 150°C$ are generally smaller than the SMD values for $T_w = 20°C$. This behavior is attributed in part to the thickness of the fuel film along the wall as shown in Fig. 4(g) and (h). Larger droplets are created during splashing on the unheated plate where the film thickness is greater.

It is interesting to note that the droplet diameter curves show fluctuations during the injection period which lasts

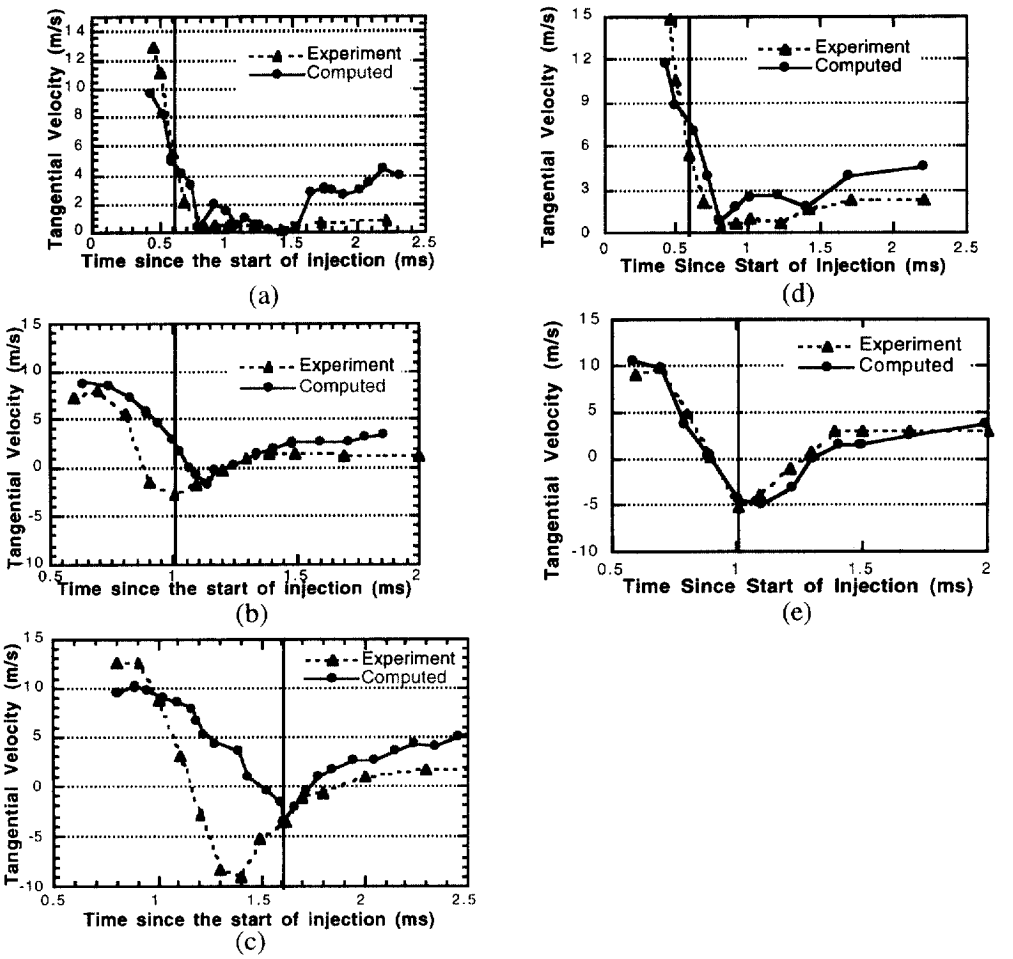

Fig. 6. Temporal history of the droplet tangential velocity at a height of 3.0 mm from the wall surface and at a radial distance of (a) 6 mm and $T_w = 20$°C, (b) 10 mm and $T_w = 20$°C, (c) 15 mm and $T_w = 20$°C, (d) 6 mm and $T_w = 150$°C, and (e) 10 mm and $T_w = 150$°C.

1.0 ms. Trends on the whole are decreasing with radial distance. However, some values at downstream positions ($r = 15$ mm and $h = 0.5$ mm) are comparatively larger than those upstream ($r = 6$ mm and $h = 0.5$ mm). A possible explanation for the presence of larger droplets downstream is droplet collision and coalescence. In particular, the SMD for $T_w = 150$°C is larger than $T_w = 20$°C (see Fig. 7(b) and (e), Fig. 8(b) and (e)) after the passage of the wall vortex. Based on the simulations, the stronger vortex for $T_w = 150$°C entrains a larger number of droplets, thus increasing the collision frequency resulting in an increase in coalescence behind the wall vortex.

In general, as the distance from the wall surface increases, the droplet size decreases. This provides further evidence that the majority of the droplet momentum remains concentrated in the region near the wall surface.

In an attempt to better understand the behavior observed in the droplet tangential velocities shown in Fig. 6, the location and velocity of the wall vortex are shown in Fig. 8 for both wall temperatures. To estimate the convective velocity of the wall vortex, Arcoumanis and Chang performed measurements of the normal component of velocity of the droplets at a height of 5.0 mm at various radial locations. The center of the vortical structure was determined by the position where the normal velocity is zero, thus allowing the estimation of the arrival time of the vortex at each radial position. From the computed and experimental approximations of the convective velocity of the vortex, the velocity for the high wall temperature case is greater than the low wall temperature case and with near constant velocity. In contrast, the low wall temperature vortex decays with increasing radial distance. From this information, the oscillatory behavior of the tangential velocity is attributed to the wall vortex moving radial through the measuring volume. For example, the wall vortex passes

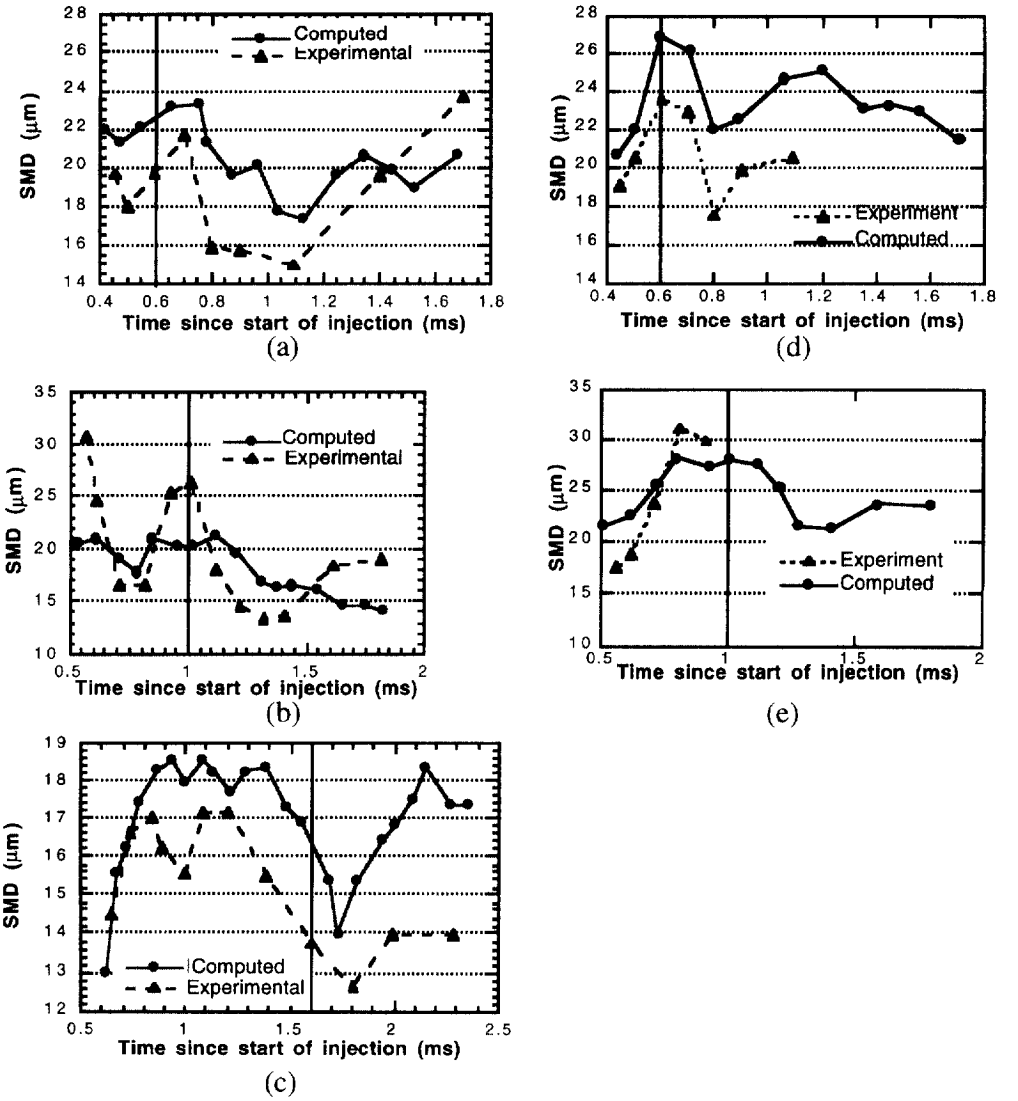

Fig. 7. Temporal history of the mean droplet diameter at a height of 0.5 mm from the wall surface and at a radial distance of (a) 6 mm and $T_w = 20$°C, (b) 10 mm and $T_w = 20$°C, (c) 15 mm and $T_w = 20$°C, (d) 6 mm and $T_w = 150$°C, and (e) 10 mm and $T_w = 150$°C.

through the point at a height of 3.0 mm and a radial distance of 10 mm at a time of 1.1 ms for both the experimental and computational data. From Fig. 6(b), the droplets experience a reversal in direction between the times of 0.9–1.2 ms for the experimental data and 1.0–1.2 ms for the computational data. These times agree with the time the vortex is believed to pass through this point.

Based on the measurements of the normal velocity component of the droplets at a height of 5.0 mm above the surface and measured between radial distances of 10 and 20 mm over a 50 μs time interval, Arcoumanis and Chang calculated an estimate of the mass flowrate of air entrained into the wall-jet. By assuming symmetry about the spray axis, the investigators evaluated the entrained mass flowrate using the expression:

$$\dot{m} = \int_{r=10}^{r=20} \rho_{air} 2\pi r V_n \, dr \tag{33}$$

where V_n is the droplet normal velocity, ρ_{air} is the air density and r is the radial distance from the spray axis. The mass flowrate is calculated using KIVA in a similar manner as equation (33) except that the gas normal velocity is used instead of the droplet normal velocity. The results, which are shown in Fig. 9, reveal that initially the mass flowrate is negative due to the passage of the wall-

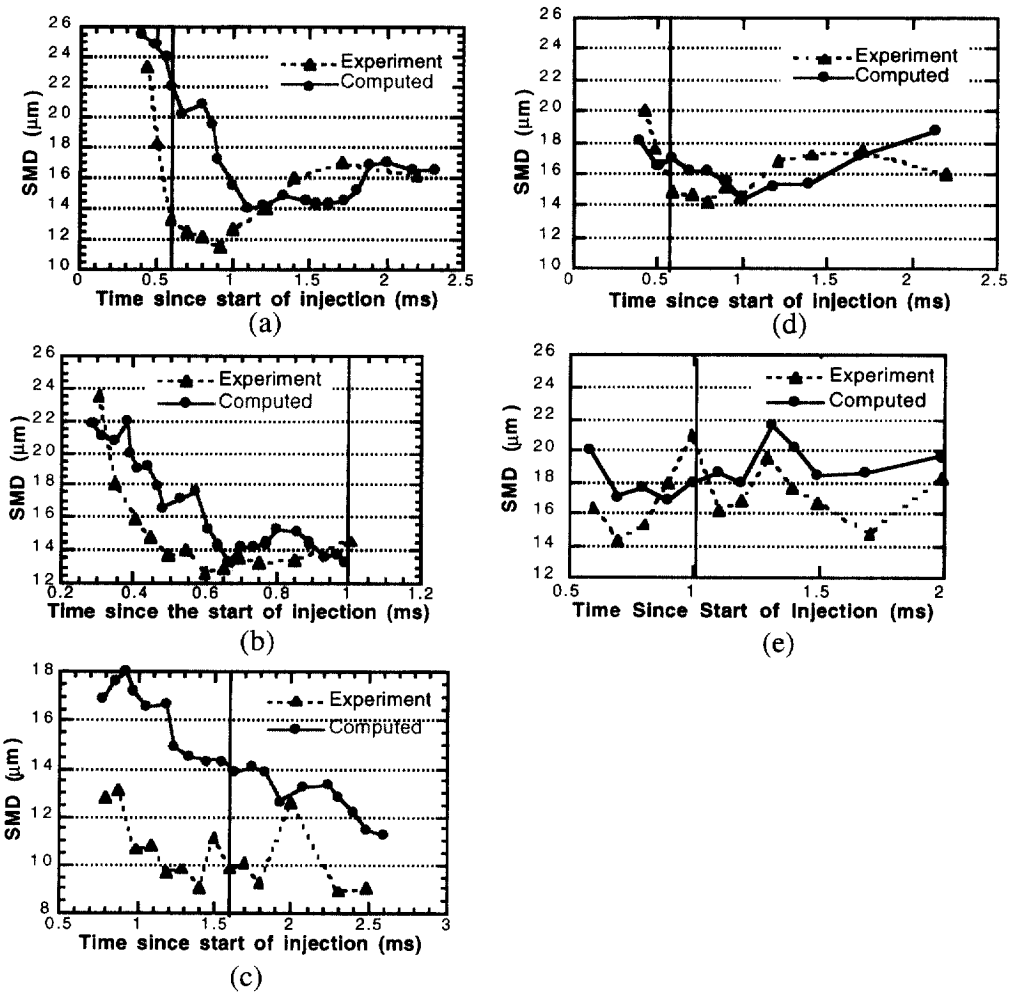

Fig. 8. Temporal history of the mean droplet diameter at a height of 3.0 mm from the wall surface and at a radial distance of (a) 6 mm and $T_w = 20$ C, (b) 10 mm and $T_w = 20$ C, (c) 15 mm and $T_w = 20$ C, (d) 6 mm and $T_w = 150$ C, and (e) 10 mm and $T_w = 150$ C.

jet head that pushes the air away from the wall. Later, positive entrainment of the air starts and becomes significant at times greater than 1.5 ms. Thus, this wall vortex structure passing through the domain also effects the air entrainment into the spray structure. Additionally, the entrainment of air increases with wall temperature. Air entrainment into the wall-jet occurs earlier for the high temperature case. This tends to suggest that the higher wall temperature promotes more air entrainment into the wall-jet, thus enhancing fuel–air mixing in impinging transient diesel sprays.

9. Conclusions

In an attempt to account for the fuel distribution along the surfaces of IC engines, a fuel film model has been formulated using thin film assumptions. This is achieved by solving the continuity, momentum, and energy equations for the 2-D film that flows over a 3-D surface. Important features of the model include mass and momentum contributions to the film due to spray drop impingement, splashing (secondary atomization), interfacial shear, piston acceleration, dynamic pressure, conduction, and convective heat and mass transfer.

In order to adequately represent drop interaction processes on a subgrid scale, impingement regimes and post-impingement behavior have been modeled using experimental data and mass, momentum, and energy conservation constraints. The regimes modeled for spray–film interaction are stick, rebound, spread and splash.

The fuel film and spray–wall models are validated through a series of comparisons to wall spray experimental data. The models provided good agreement for

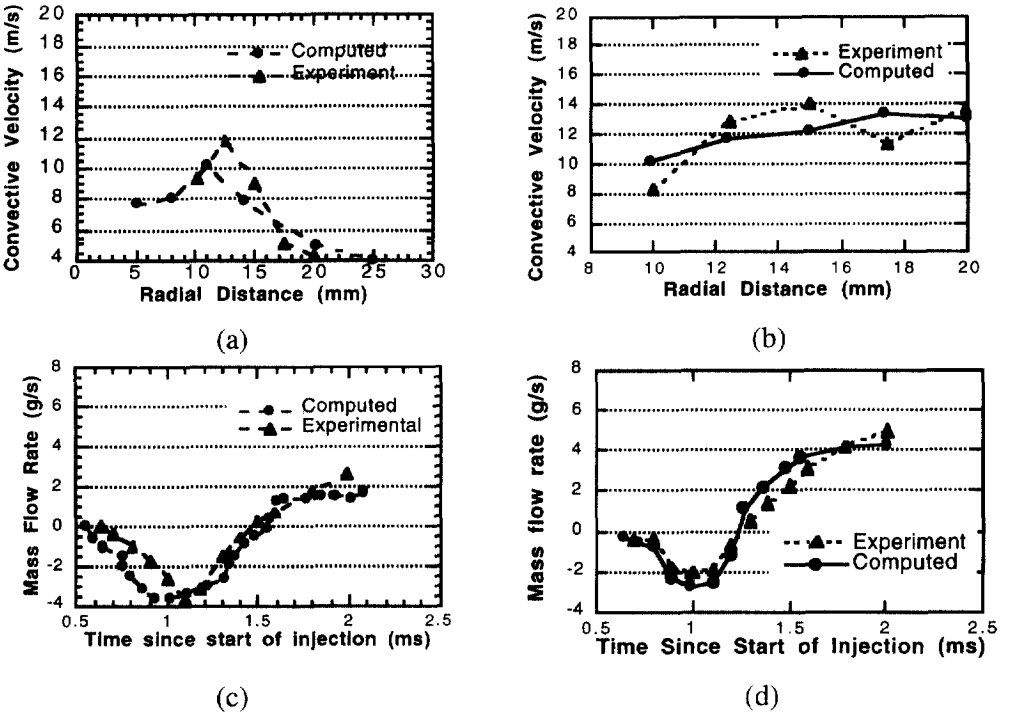

Fig. 9. Calculated air entrainment rate into the wall-jet integrated over the radial distance between 10 mm and 20 mm for a wall temperature of (a) $T_w = 20$ C and (b) $T_w = 150$°C. Comparison of the calculated wall vortex convective velocity along the wall for a wall temperature of (c) $T_w = 20$°C and (d) $T_w = 150$°C.

wall spray radius and height, film thickness, film spreading radius, and percentage of fuel that adheres to the wall. As for secondary droplet characteristics, the models capture the correct trends for drop sizes and velocities over the majority of the injection period. Additionally, the simulations have demonstrated the influence of the wall vortex on spray–wall interactions. Consequently, the models provide a predictive means of determining spray-wall interactions with the eventual formation of liquid films that can be used for multi-dimensional simulations of IC engines.

Acknowledgements

This material is based upon work supported by, or in part by, the U.S. Army Research Office under grant number DAAH04-94-G-0328. The authors would like to thank Peter Senecal and Professor Rolf Reitz for helpful suggestions for the improvement of this work.

References

[1] Rein M. Phenomena of liquid drop impact on solid and liquid surfaces. Fluid Dynamics Research 1993;12:61–93.

[2] Prosperetti A, Oguz HN. The impact of drops on liquid surfaces and the underwater noise of rain. Annual Rev Fluid Mechanics 1993;25:577–602.

[3] Bardon MF, Rao VK, Gardiner DP. Intake manifold fuel film transient dynamics. SAE Technical Paper Series, 870569, 1987.

[4] Kay IW. Manifold fuel film effects in an SI engine. SAE Technical Paper Series, 780944, 1978.

[5] Yoshikawa Y, Nakada T, Itoh T, Takagi Y. Numerical simulation system for analyzing fuel film flow in gasoline engine. SAE Technical Paper Series, 930326, 1993.

[6] Cartellieri WP et al. Status report on a preliminary survey of strategies to meet US-1991 HD diesel emission standards without exhaust gas after treatment. SAE Paper 870343, 1987.

[7] Welberger P, Cartellieri WP. Fuel injection and combustion phenomena in a high speed DI diesel engine observations by means of endoscopic high speed photography. SAE Technical Paper Series, 870097, 1987.

[8] Gonzalez D, Gonzalez MA, Borman GL, Reitz RD. A study of diesel cold starting using both cycle analysis and multidimensional calculations. SAE Technical Paper Series, 910180, 1991.

[9] Naber JD, Farrell PV. Hydrodynamics of droplet impingement on a heated surface. SAE Technical Paper Series, 930919, 1993.

[10] Zhengbai L, Jingwei Z, Yueshang L. Experimental investigation of film space atomization combustion in D.I. diesel engines. SAE Technical Paper Series, 901578, 1990.

[11] O'Rourke P, Amsden A. A particle numerical model for wall film dynamics in port-injection engines. SAE Technical Paper Series, 961962, 1996.
[12] Himmelbauch J, Noll B, Witting S. Experimental and numerical studies of evaporating wavy fuel films in turbulent air flow. Int. J. Heat Mass Transfer, 1994;37(8):1217–26.
[13] Stanton DW, Rutland CJ. Modeling fuel film formation and wall interaction in diesel engines. SAE Technical Paper Series, 960628, 1996.
[14] Stanton DW, Rutland CJ. Multi-dimensional modeling of fuel films in direct injection diesel engine. ASME Internal Combustion Engine Fall Conference, Madison, WI, 1997.
[15] Sattelmyer T, Wittig S. Performance characteristics of pre-filming airblast atomizers in comparison with other airblast nozzle. Encycl of Fluid Mechanics 1989;8.
[16] Sill KH. Wärme- und Stoffübergang in turbulenten Strömungsgrenz schichten längs verdunstender welliger Wasserfilme, Dissertation, Universität Karlsruhe, Institut für Thermische Strömungsmachinen, 1982.
[17] Zhbankova SL, Kolpakov AV. Collision of water drops with a plane water surface. Fluid Dyn. 1990;25(3):470–73.
[18] Stanton DW, Rutland CJ. Multi-dimensional modeling of heat and mass transfer of fuel films resulting from impinging sprays, submitted, SAE Technical Paper Series, 1998.
[19] Rodrigues F, Mesler R. Some drops don't splash. Journal of Colloid and Interface Science 1985;106(2):347–52.
[20] Jayaratne OW, Mason BJ. The coalescence and bouncing of water drops at an air/water interface. Proc R Soc London 1964;A280:545–65.
[21] Stow CD, Hadfield MG. An experimental investigation of fluid flow resulting from the impact of a water drop with an unyielding dry surface. Proc R Soc Lond 1981;A373:419–41.
[22] Matsumoto S, Saito S. On the mechanism of suspension of particles in horizontal conveying: Monte Carlo simulation based on the irregular bounding model. J Chem Engng Japan 1970;3:83–92.
[23] Naber JD, Reitz RD. Modeling engine spray/wall impingement. SAE Technical Paper Series, 880107, 1988.
[24] Stow CD, Stainer RD. The physical products of a splashing water drop. Journal of the Meteorological Society of Japan 1977;55(5):518–31.
[25] Levin Z, Hobbs PV. Splashing of water drops on solid and wetted surfaces: hydrodynamics and charge separation. Phil Trans R Soc London 1971;A269:555–85.
[26] Yarin AL, Weiss DA. Impact of drops on solid surfaces: self-similar capillary waves, and splashing as a new type of kinematic discontinuity. J Fluid Mech 1995;283:141–73.
[27] Mundo Chr, Sommerfeld M, Tropea C. Droplet-wall collisions: experimental studies of the deformation and breakup process. Int J Multiphase Flow 1995;21(2):151–73.
[28] Amsden AA, O'Rourke PJ, Butler TD. KIVA: a computer program for two- and three-dimensional fluid flows with chemical reactions and fuel sprays. Los Alamos Report No. LA-11560-MS, 1989.
[29] Reitz RD, Rutland CJ. Development and testing of diesel engine CFD models. Prog Energy Combust Sci 1995;21:173–96.
[30] Rutland CJ, Eckhause J, Hampson G, Hessel R, Kong S, Patterson M, Pierpont D, Sweetland P, Tow T, Reitz RD. Toward predictive modeling of diesel engine intake flow, combustion, and emissions. SAE Technical Paper Series, 941897, 1994.
[31] Saito GT, Suzuki T, Tokuoka N. Experimental study on the behavior of the drop impinging on a hot surface. JSME No. 84-0161 A. 1985. p. 84.
[32] Arcoumanis C, Chang JC. Flow and heat transfer characteristics of impinging transient diesel sprays. SAE Paper 940678, 1994.
[33] Arcoumanis C, Cassali EC, Paál G, Whitelaw JH. Transient characteristics of multi-hole diesel sprays. SAE Paper 900480, 1990.